Confocal fluorescence microscope with dual-axis architecture and biaxial postobjective scanning

Thomas D. Wang
Christopher H. Contag
Stanford University School of Medicine
Stanford, California 94305
E-mail: tdwang@stanford.edu

Michael J. Mandella
Ning Y. Chan
Optical Biopsy Technologies, Inc.
Palo Alto, California 94301

Gordon S. Kino
Stanford University
Edward L. Ginzton Laboratory
Stanford, California 94305

Abstract. We present a novel confocal microscope that has dual-axis architecture and biaxial postobjective scanning for the collection of fluorescence images from biological specimens. This design uses two low-numerical-aperture lenses to achieve high axial resolution and long working distance, and the scanning mirror located distal to the lenses rotates along the orthogonal axes to produce arc-surface images over a large field of view (FOV). With fiber optic coupling, this microscope can potentially be scaled down to millimeter dimensions via microelectromechanical systems (MEMS) technology. We demonstrate a benchtop prototype with a spatial resolution $\leqslant 4.4$ μm that collects fluorescence images with a high SNR and a good contrast ratio from specimens expressing GFP. Furthermore, the scanning mechanism produces only small differences in aberrations over the image FOV. These results demonstrate proof of concept of the dual-axis confocal architecture for *in vivo* molecular and cellular imaging. © *2004 Society of Photo-Optical Instrumentation Engineers.* [DOI: 10.1117/1.1760760]

Keywords: confocal; microscope; fluorescence; molecular biology; imaging; *in vivo*.

Paper 03088 received Jul. 1, 2003; revised manuscript received Dec. 19, 2003; accepted for publication Dec. 19, 2003.

1 Introduction

Confocal microscopy is a powerful tool for imaging in biological tissue, and can be used *in vivo* if the lenses and scanning mechanisms can be made sufficiently small. This method performs optical sectioning in a highly scattering media with subcellular resolution, a high signal-to-noise ratio (SNR), and a good contrast ratio,[1] an achievement not easily matched by any other imaging modality. Also, molecular structures can be identified by fluorescence markers to reveal previously unobservable details about biological processes *in vivo*. In addition, a microscope implanted in an animal model can perform longitudinal studies over time, thus preserving experimental continuity and reducing the number of sacrificed animals. Currently, *in vivo* confocal imaging is performed on exposed tissue surfaces such as that of skin or from tissue exposed surgically.[2–6] Internal access to tissue is limited by the large physical dimensions of conventional microscopes objectives. A numerical aperture (NA) of at least 0.75 is required to achieve an axial resolution of a few micrometers, the dimensions necessary to resolve molecular and subcellular structures.[7] In the conventional single-axis configuration, the same lens is used for illumination and image collection, and the optics cannot be reduced to millimeter scale without sacrificing resolution, field of view (FOV), or working distance (WD). Also, because the scanning mechanism is located proximal to the objective, multiple optical elements are re-

quired to correct for aberrations and achieve high performance. Furthermore, the use of standard objectives *in vivo* is rather cumbersome.

Previously, a laser scanning confocal microscope with single axis configuration has been miniaturized with microelectromechanical systems (MEMS) technology.[8,9] This instrument uses a single-mode optical fiber as the pinhole, and the optical path is folded into a zigzag pattern by a silicon spacer coated with reflective surfaces, resulting in a scanhead size of $1.2 \times 2.5 \times 6.5$ mm. The axial resolution of 18 μm was not adequate for *in vivo* use, and the binary lens objective was too dispersive to collect fluorescence. We previously described the dual-axis architecture and demonstrated proof of concept with reflectance images.[10] Also, we have shown the ability of the dual-axis configuration to differentiate against noise from scattering over a depth of 1 mm using illumination at 1345 nm. These reflectance images were vertical cross sections collected perpendicular to the tissue surface using uniaxial postobjective scanning,[11] and were achieved with low-coherence heterodyne detection. We now demonstrate fluorescence (noncoherent) images collected in horizontal crosssections parallel to tissue surface using biaxial postobjective scanning.

The collection of fluorescence images *in vivo* can be used to study transgenic models to answer a diverse range of biological questions.[12,13] Molecules can be tagged with fluorescence reporters to enhance the image contrast and reveal details about important biological processes such as cell transport, tumor formation, and development. GFP is an example marker of gene expression and protein targeting in vi-

Address all correspondence to Dr. Thomas D. Wang, Stanford Univ. School of Medicine, CCSR Bldg, Rm. 3115, 269 Campus Dr., MC: 5187, Stanford, CA 94305-5187. Tel: 650-723-0725; Fax: 650-723-5488; E-mail: tdwang@standford.edu
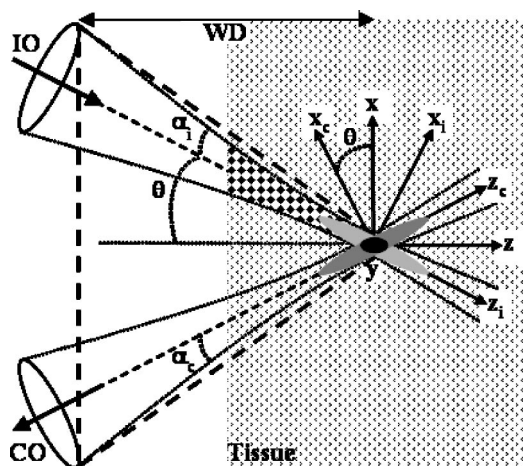
Fig. 1 Dual-axis architecture uses separate low-NA objectives for illumination (IO) and collection (CO) at angle θ to the z axis, creating a long WD. The illumination path for dual-axis (checkered region) results in reduced noise from scattered light compared with that from a single axis (area within dashed lines).

able cells and organisms. In addition, the distribution of GFP within the cell can be modulated posttranslationally by the biochemical environment and by protein-protein interactions.[14] Two or more variants of GFP can be used to provide multiple labels of subcellular processes.[15] Furthermore, the combination of two GFPs enable fluorescence energy transfer (FRET) that is sensitive to the orientation and distance on a nanometer scale between two fluorophores.[16] These types of processes may be observed *in vivo* with multiphoton imaging[17,18] upon successful development of hollow fibers. In addition, GFP has been used to monitor the development of mammalian embryos[19–21] and the development of metastatic tumors.[22–24]

2 Dual-Axis Architecture

The dual-axis architecture uses separate low-NA objectives for illumination (IO) and collection (CO),[25–28] as shown in Fig. 1. The NA of each lens is determined by the angles α_i and α_c. The point spread function of either objective (gray ovals) has a long axial but narrow transverse dimension. The overall axial resolution of the system is represented by the length of the overlapping region (black oval). The length of this overlap depends primarily on the transverse rather than the axial dimension of the beams at the focus. The illumination beam is incident to the tissue at angle θ, and the fluorescence originating from the overlapping focal volume at the intersection of the two beams, is collected off-axis. As a result, light scattered along the illumination path (checkered region) outside of the focal volume is unlikely to arrive at the collection objective with the proper angle necessary for detection because the correct combination of scattering events required occurs with low probability.[11] On the other hand, a standard confocal microscope objective has a single axis and requires a much higher NA to achieve an equivalent axial resolution. As a result, the light collected emerges from within the same large-angle cone (dashed lines) as that traversed by the illumination, thus resulting in increased noise from scattering.
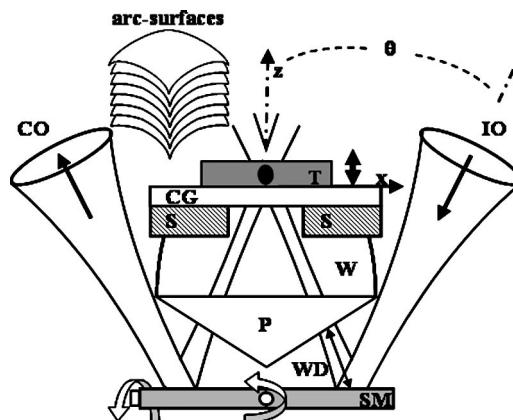

Fig. 2 Schematic with the biaxial postobjective SM located distal to objectives to create images along arc-surfaces within tissue (T) placed on a cover glass (CG) that is sitting on a stage (S). The bead of water (W) provides index matching.

3 Biaxial Postobjective Scanning

We use a novel method of scanning whereby the illumination and collection beams pass through their respective objectives on-axis, independent of the angle of the scan mirror, and a single plane biaxial mirror located distal to the objectives is used to steer the beam, as shown in Fig. 2. With the mirror in this location, we define the scanning distance (SD) as the displacement between the mirror surface and the focal volume. Note that this parameter is different from the WD (defined in Fig. 1). In the biaxial mode, the scanning mirror (SM) rotates about both the x and y axes and scans the illumination and collection beams synchronously in a manner such that the intersection of the two axes remains oriented at a constant angle of 2θ. The focal volume remains overlapped and moves without changing shape over an arc surface within the tissue. This feature can be conceptualized by regarding this optical system as being equivalent to the outer annular ring of a high-NA objective illuminated with two parallel collimated beams. The two separate beams are focused with a low NA, and a single plane mirror distal to the objective can steer the beams together and preserve the dimensions of the overlapping focal volume as long as no aberrations are introduced, a good approximation when the maximum angle of deflection during scanning is small compared to θ. Note that it would be difficult to use postobjective scanning with a conventional single axis microscope because of the short WD. Because the two separate beams are incident to the tissue at an angle, a Teflon amorphous fluoropolymer (AF) prism (P), $n = 1.31$, is placed in the optical path to reduce the aberrations that occur from the beam being incident at an angle to the tissue. Note that because the two beams are not scanned through the objectives, corrective elements are not required proximally, and simple, low-NA lenses that are easy to miniaturize can be used.

4 System Design

We constructed a benchtop prototype with an inverted configuration, as shown by the schematic in Fig. 3. The axes of illumination and collection are oriented at $\theta = 30$ deg to the midline. A frequency-doubled semiconductor laser (Coherent

Sapphire) delivers illumination at $\lambda = 488$ nm into a single-mode polarization-maintaining (PM) optical fiber SMF_1 with a mode field diameter (MFD) of 2.9 μm and NA=0.11. The polarized light from the fiber is collimated and focused by two gradium lenses L_1 (25 mm diameter, focal length $f = 60$ mm) and L_2 (10 mm diameter, $f = 30$ mm). The illumination aperture of L_2 is overfilled to approximate uniform illumination and thereby reduces the illumination spot size. From the expanded view in Fig. 2, the specimen sits on a CG that rests on stage (S) whose height is adjusted by a piezoactuator with submicrometer accuracy. The bead of water (W) reduces the mismatch in refractive index in the space between the prism and the tissue. The CG represents a mismatch in refractive index between water and tissue, and introduces aberrations such as coma and astigmatism. To focus deeper into the tissue, we lower the height of the CG, and the space filled with water decreases. Since water and tissue have almost the same refractive index, the total optical path length (OPL) of the illumination and collection beams remains approximately constant, thus avoiding defocus and misalignment of the beams at different imaging depths. The scanning distance of the system beyond the scanning mirror is ~ 19 mm.

Biaxial scanning is obtained simultaneously by driving the scan mirror (GSI Lumonics) with a 50-Hz sinusoidal waveform and a 0.1-Hz linear ramp waveform along the fast and slow axes, respectively, resulting in a raster scan having a FOV of ~ 500 μm after clipping the nonlinear portions at the edges of the sinusoidal scan. The fluorescence generated from the tissue is collected by a pair of achromats L_3 and L_4 (25 mm diameter, $f = 50$ mm), which collimate and focus the beam into a second single-mode fiber SMF_2 with MFD of 3.4 μm and NA=0.11. A long-pass filter (LPF) with a sharp cutoff at 505 nm blocks the excitation light, and fluorescence is detected by the photomultiplier tube (PMT, Electron Tubes 9125SB). The detection bandwidth of the preamp (PA) is 60 kHz, the images are digitized [with an analog-to-digital converter (ADC)] in dc-coupled variable scan mode (Data Translation DT3152) using DT Vision Foundry software to 480 $\times$ 480 pixels. The image was centered by adjusting the horizontal synchronization with a digital delay (SRS DG535), and displayed on a computer (PC). By removing the LPF, we can also collect reflectance images that are spatially coregistered with that of the fluorescence images using the dichroic mirror (DM) and silicon detector (D).

5 Materials and Methods

5.1 Biaxial Scanning

The fluorescence images were collected with the specimen placed in a single well-chambered CG made from #1 German borosilicate (~ 160 μm thick). The power incident on the specimen was ~ 500 μW. Each image was collected in 10 s, and averaged over nine frames to improve the SNR. Images were collected over a range of axial depths by adjusting the piezoactuator. The SNR at a given point in the image was determined by taking a ratio of the mean intensity and the standard deviation of the surrounding 3×3-pixel array. The contrast ratio between two regions of tissue was determined by dividing the mean intensity of three sites in one region with that of three sites in the other.

The effect of aberrations created by biaxial postobjective scanning was calculated by ray trace analysis of the illumination half of the optical system using Zemax, an optical modeling software. In this simulation, rays of light at wavelength $\lambda = 488$ nm emerge from the single-mode illumination fiber as a spherical wavefront over a range of angles spanning the fiber NA. The SM is deflected ± 0.5 deg in either direction to deflect the beam over a FOV of 600×600 μm^2. After collimation and focusing, the converging rays pass through the air, 3 mm of the Teflon AF prism, 1 mm of water, a 160-μm CG, and finally through 300 μm of tissue before coming to a focus (see Fig. 2). The deviation of the aberrated wavefront from an ideal spherical wavefront is calculated at nine positions arranged in a 3×3 array of object illumination points in the x and y directions spanning the FOV of the image. The wavefront aberration at each point is defined as the peak-to-valley, or worst, deviation from the ideal spherical wavefront at the exit pupil of the optical system.

5.2 DSH-293 GFP Cells

Stable cell lines of DSH-293 cells were first transfected with an enhanced GFP (S65T) reporter expressed from a cytomeglovirus (CMV) promotor on a plasmid containing a neomycin resistance gene.[29] After transfection via lipofectamine (Invitrogen Life Technologies) per manufacturer's recommendations, transfected cells were selected in G418 and sorted by fluorescence-activated cell sorter (FACS) for fluorescence intensity. A monolayer of cells was grown on a chambered CG, and covered with media. In the dual-axis, the illumination intensity (energy per unit volume) was ~ 0.3 mJ/μm^3. For purposes of comparison, fluorescence images were also collected with a conventional single-axis confocal microscope (Bio-Rad MRC 1024) using a 1.2-NA oil immersion lens. This objective has transverse and axial resolutions of 0.4 and 0.9 μm, respectively, and a WD of ~ 100 μm. A neutral density filter was used to adjust the excitation power at 488 nm to ~ 500 μW, and the frame collection time was 1 s. These parameters resulted in an intensity of ~ 3 mJ/μm^3.

5.3 Transgenic GFP Mouse Model

A transgenic mouse that expresses GFP under the control of a β-actin-CMV promoter-enhancer[30] was sacrificed, and the cerebellum was excised and divided sagitally on either side of the vermis. The cortex was placed face down on the cover glass and covered with a drop of fluorescence mounting medium (Vectashield) for index matching. Horizontal scans were collected at increasing axial depths up to ~ 100 μm, beyond which no signal was detected. On completion of imaging, the specimen was immersed in 10% formalin and processed for standard histology. Similarly, skeletal muscle was excised from the quadriceps of the transgenic mouse model, and placed on the chambered CG and covered with Vectashield. Horizontal scans were collected up to an axial depth of ~ 200 μm.

5.4 GFP Drosophila Embryos

Fluorescence images from *Drosophila melanogaster* embryos that expressed the engrailed gene labeled with GFP, a marker of developmental regulation,[31] were also collected. Engrailed
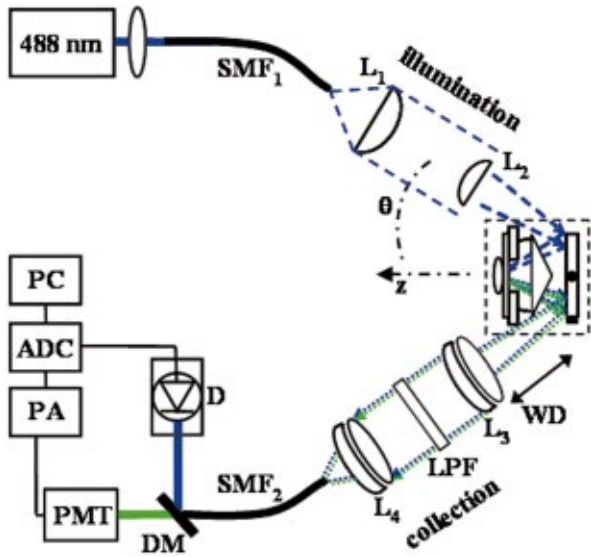
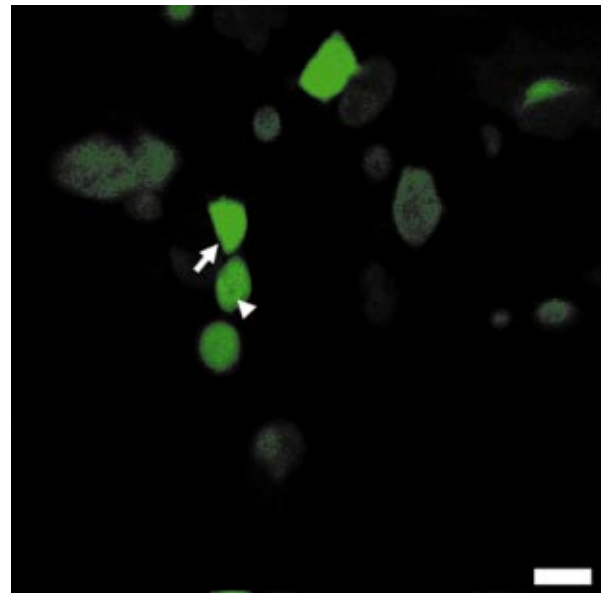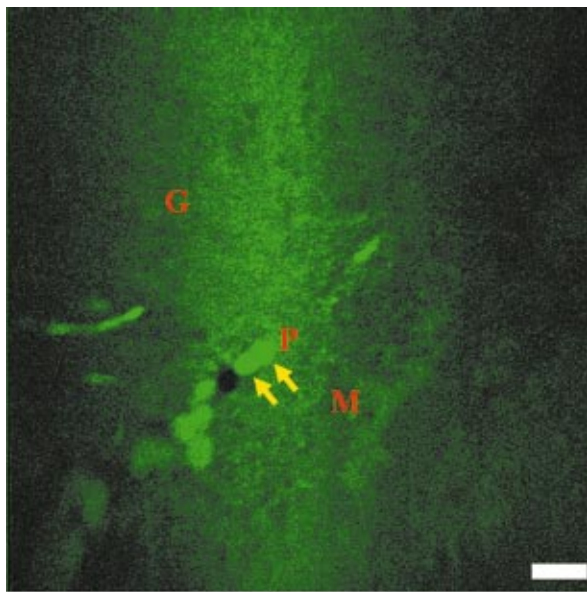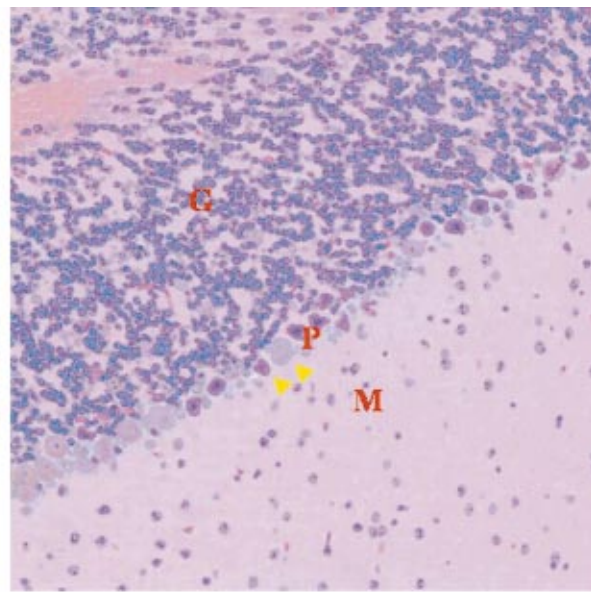Fig. 3 Schematic of dual-axis prototype details are discussed in text.

Fig. 5 Fluorescence image of DSH-293 cell monolayer demonstrates high SNR and resolution. Nuclei (arrowhead) and cell borders (arrow) can be distinguished; FOV is 500 μm and scale bar is 50 μm.

(a)

(b)

Fig. 6 (a) Fluorescence image from mouse cerebellar cortex showing Purkinje (P) cell bodies (arrows) separating the granule (G) and molecular (M) layers where FOV is 500 μm and scale bar is 50 μm, and (b) corresponding H&E section.
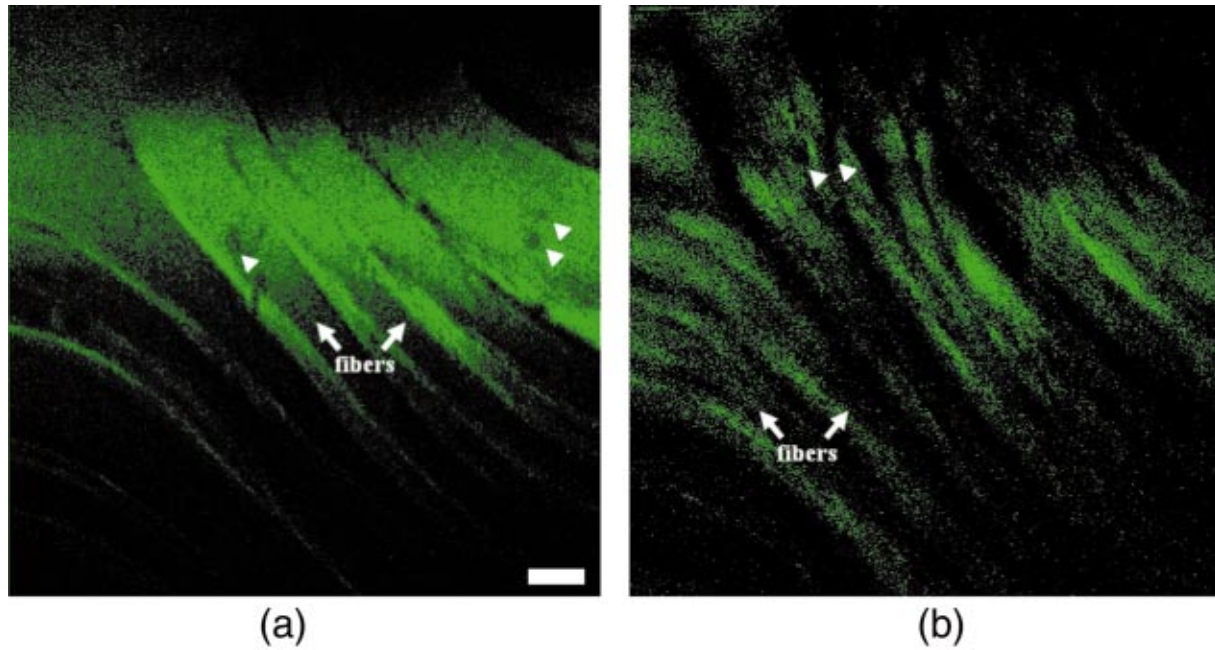
Fig. 7 Fluorescence images from mouse quadriceps show nuclei (arrowheads) and muscle fibers (arrows) at axial distance of (a) $z=0$ and (b) $z=100$ μm, with a scale bar of 50 μm.
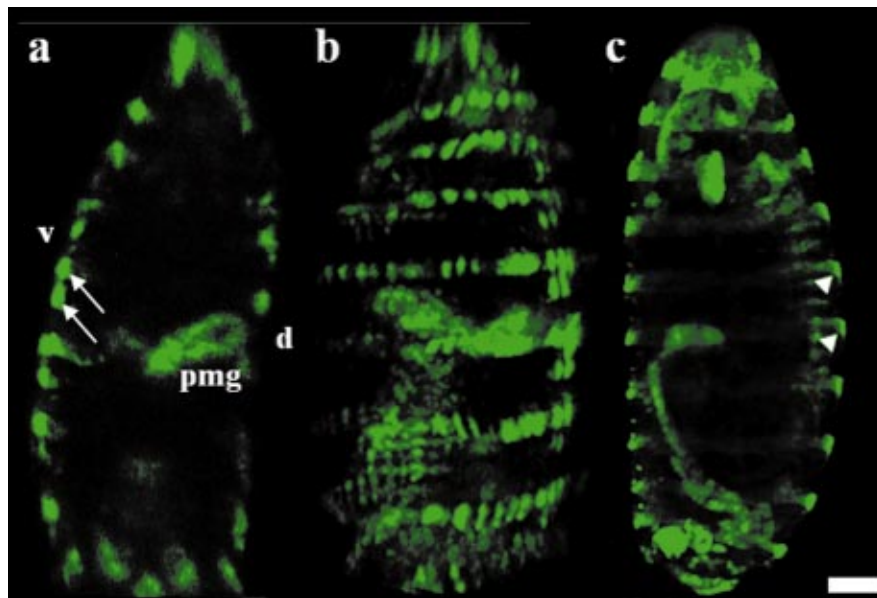

Fig. 8 Fluorescence images of *Drosophila* embryo expressing stripes of engrailed collected at a depth of $z=100$ μm with (a) dual axes (arrows) followed by (b) 2-D projection of a 3-D reconstructed image, and (c) single axis confocal microscope (arrowheads); the scale bar is 50 μm.

Table 1 WAs as a fraction of λ for an array of points spanning the image FOV.

| | *x* | | |
y	− 300	0	300
− 300	1.04	0.91	0.81
0	0.96	0.84	0.74
300	1.04	0.91	0.81

is driven by the UAS/GAL4 promoter-enhancer system, and is expressed as stripes on the outer surface of the embryo.[32] Embryos in stages 10 and 11 were rinsed with tap water, and then soaked in 50% bleach to remove the chorion. Live embryos were then placed on the chambered CG with a drop of Vectashield. The embryos are cylindrical in shape with dimensions of $\sim 200\ \mu m$ in diameter by $\sim 500\ \mu m$ in length. A series of transverse 2-dimensional (2-D) scans were collected at increasing axial depths in 10-μm increments through the thickness of the embryo, and 3-dimensional (3-D) reconstructed images were created using Amira volume modeling software. Fluorescence images were also collected with a conventional single-axis confocal microscope (Bio-Rad MRC 1024) for comparison.

6 Results

6.1 Biaxial Scanning

The wavefront aberration (WA) calculated for the array of object illumination points at the nine representative scan positions given by x and y coordinates of -300, 0, and 300 μm is shown in Table 1. The results reveal that the WA increases in the $-x$ direction (from 0.74λ to 0.96λ in the outer rows and from 0.81λ to 1.04λ in the center row), and decreases in the x direction. Furthermore, the WA increases as the beam moves along either the y or $-y$ direction, but not to the same extent as that along the x direction. The maximum difference in the WA for any two points is 0.30λ, thus biaxial postobjective scanning does not produce significant differences over the image FOV. The relative aberrations induced by the changing scan angle can be seen in the reflectance image of a standard resolution test chart, shown in Fig. 4. The set of horizontal bars resolved by scanning in the yz plane (arrow) appear sharper and narrower than the vertical bars, which are resolved by scanning along the xz plane (arrowhead). The smallest group of parallel bars oriented in either direction can be resolved, representing a transverse resolution better than 4.4 μms. Note also that the reflected intensity is most prominent near the center of the image than in the periphery. This effect is produced by the intersection of the arc surface produced by biaxial postobjective scanning with the plane surface of the test chart.

6.2 DSH-293 Cells Expressing GFP

A fluorescence image of a monolayer of DSH-293 cells expressing GFP is shown in Fig. 5. The cytoplasm appears bright and the cell has sharp borders. The nuclei (arrows) can
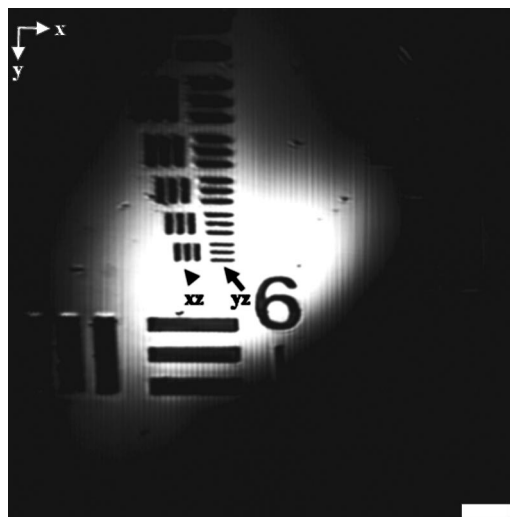

Fig. 4 Reflectance image collected with standard resolution test chart (scale bar 50 is μm). Better resolution is observed for scanning in yz plane (arrow) compared to xz plane (arrowhead). The bright region in the center is created by intersection of arc surface with plane target.

be distinguished by the relative absence of fluorescence. The SNR of the cytoplasm is 13 ± 5, and the contrast ratio between the cytoplasm and nuclei is 1.6. Fluorescence images were also collected from these cells with the single-axis confocal microscope, and resulted in an SNR of 12 ± 6 from the cytoplasm, and a contrast ratio between the cytoplasm and nuclei of 1.8. However, because low-NA lenses are used with dual-axis, the illumination intensity and light collection efficiency are not as high, and longer integration times are required. There was no evidence of photobleaching at these fluences for either microscope. A comparison of the image parameters between the dual-axis and single-axis microscopes is shown in Table 2.

6.3 Transgenic GFP Mouse Model

A fluorescence image collected from mouse cerebellum at a depth of $z = 30\ \mu m$ is shown in Fig. 6(a). Larger round structures (arrows) with high fluorescence intensity, $\sim 20\ \mu m$ in diameter, are consistent with Purkinje cell bodies and are seen

Table 2 Comparison of the performance between the dual-axis and single axis confocal microscopes.

Parameter	Dual Axes	Single Axis
NA	0.11	1.2
Power (mW)	0.50	0.50
Collection time (s)	90	1.0
Resolution (μm)	4	0.4
SNR	13 ± 5	12 ± 6
Contrast ratio	1.6	1.8
Distance (mm)	19	0.1

Table 3 Summary of SNRs and contrast ratios for the fluorescence collected from several transgenic specimens expressing GFP.

Parameter	Depth (μm)	SNR	Contrast Ratio
DSH-293 cells	0	13 ± 5	1.6
Purkinje cell bodies	30	13.1 ± 0.5	3.1
Muscle cells	0	4.8 ± 0.5	3.5
Drosophila embryos	100	15 ± 3	115

aligned side by side in a row. The corresponding H&E (hematoxylin and eosin) section shown in Fig. 6(b) shows three layers. The granule (G) layer (upper diagonal half) demonstrates dense cellularity, the intervening Purkinje (P) layer reveals several aligned neuronal cell bodies (arrowheads), and the molecular (M) layer (lower diagonal half) contains relatively few cells. From fluorescence, the SNR for the Purkinje cells and molecular and internal granule layers is 13.1 ± 0.5, 4.4 ± 0.3, and 4.3 ± 0.4, respectively. The contrast ratio between the Purkinje cells and that of the molecular layer and internal granule layer is 3.0 and 3.1, respectively. In addition, fluorescence images of skeletal muscle from the quadriceps at $z = 0$ and 100 μm are shown in Figs. 7(a) and 7(b), respectively. Individual muscle fibers (arrows) and cell nuclei (arrowheads) can be seen. At $z = 0$, the SNR of the cytoplasm is 4.8 ± 0.5, and the contrast ratio between the cytoplasm and nuclei is 3.5. At $z = 100$ μm, the SNR of the cytoplasm is 1.6 ± 0.3. Signal is observed above the noise floor at an axial distance up to ~ 200 μm.

6.4 *GFP Drosophila Embryos*

A fluorescence image collected from a transgenic *Drosophila* embryo at a depth of $z = 100$ μm is shown in Fig. 8(a) with a scale bar of 50 μm. There are 14 stripes of engrailed (arrows) with single lines of cells marking the posterior parts of the segments. The posterior midgut (pmg) is seen invaginating from the dorsal (d) and ventral (v) sides. The SNR of the stripes is 15 ± 3, and the contrast ratio between the stripes and the embryo protoplasm is 115. A 2-D projection of a 3-D reconstructed image from 18 horizontal sections is shown in Fig. 8(b). In the single-axis confocal image [shown in Fig. 8(c)], the stripes of engrailed have similar intensity and are equally spaced. However, in the dual-axis image, the middle stripes (arrows) are more intense and the spacing appears somewhat irregular. These differences occur because the image is collected over an arc surface rather than a plane. These differences can be corrected with appropriate image processing software, if desired. The SNRs and contrast ratios for fluorescence images collected at various depths with the dual-axis prototype are summarized in Table 3.

7 Discussion

We demonstrated a confocal microscope that collects fluorescence images from biological specimens expressing GFP using low-NA objectives with high resolution, SNR, and contrast ratio with deep tissue penetration over a large FOV. Subcellular structures such as nuclei and cell membranes can

be distinguished from cells in a monolayer and within bulk tissue specimens over axial depths of several hundred micrometers. The collection of light off-axis selects against light scattered along the illumination beam, thus reducing the image noise. Combined with fiber optic coupling, this instrument can be reduced in size to millimeter dimensions and used for *in vivo* collection of fluorescence images in transgenic models. With postobjective scanning, scaling down the dual axes architecture will change the WD and FOV, but not the image resolution. A miniature confocal microscope can be used for *in vivo* molecular and cellular imaging as a handheld device or as an implanted instrument. The long WD provides greater ease of use for imaging from the surface of the skin or from surgically exposed fields. Also, for longitudinal studies, this instrument can be inserted through an implanted cannula cemented to the outer surface of a transgenic mouse, such as the cranium, and a sterile obturator can be inserted to maintain patency of the cannula when the microscope is not in use. The microscope can be mechanically translated deeper into the tissue to image remote structures. While the imaging performance of the dual-axis does not equal to that of the single-axis instrument, these images along with its suitability for miniaturization demonstrate the potential for *in vivo* biological investigations.

The biaxial scanning mechanism and the simple objective lenses are the key features that enable scalability of the dimensions. Scanning the illumination and collection beams behind the objectives rather than in front eliminates the need for additional optical elements to correct for off-axis aberrations. Thus, we can use low-NA lenses that are simple to fabricate, low in cost, and easy to miniaturize. Furthermore, the differences in wavefront aberration created by biaxial postobjective scanning are small. The aberrations caused by misalignment are more apparent when scanning the beams across the width of the prism (xz plane) than along its length (yz plane). This occurs because scanning in the xz plane creates a larger misalignment in the overlap of the two beams, as the refraction of the separate beams at the air-prism interface occurs in the opposite direction as opposed to the same. For diffraction-limited performance, we expect the WA$<0.25\lambda$ at all points in the image; however, we do not achieve this value here because we have used readily available optics to demonstrate the proof of principle of this method. We will use custom optics for diffraction-limited performance in future systems.

Furthermore, a larger residual aberration is seen to exist in the illumination beam that is not associated with the scan position. This is a result of a combination of spherical aberration, coma, and astigmatism. The spherical aberration is caused primarily by the converging beam passing through the several-millimeter-thick layer of Teflon AF and 1 mm of water, and the coma and astigmatism is caused mostly by the 30-deg incidence angle of the beam at the slight refractive index mismatch between the water-Teflon AF interface, and the large index mismatches between the water-CG and CG-tissue interfaces. These aberrations can be improved by custom fabrication of the objective lenses, by using a prism material that is more closely matched to the index of water ($n = 1.33$), and by eliminating the cover glass, which is not needed in the miniaturized *in vivo* instrument.

For this technique to be used *in vivo* in anesthetized animals, we desire the image collection time to be less than 2 s to

avoid motion artifacts. The fluorescence images shown were collected in 90 s, an interval that can be reduced significantly by optimizing the system design. To achieve the same SNR as that in the images shown, we can increase the fluorescence detection efficiency by using (1) a PMT with a multialkali rather than bialkali photocathode, increasing the detector quantum efficiency by a factor of ~ 2 and (2) objective and optical fibers with total collection $NA > 0.20$ (compared to $NA = 0.11$), gaining a factor of ~ 4. We can also generate more fluorescence photons by (3) increasing the laser power by a factor of ~ 2; and (4) decreasing the overfill of illumination aperture, gaining a factor of ~ 4. These changes alone can increase the fluorescence signal by a factor of ~ 60. In addition, we can accept images with a lower SNR, and develop novel reporters such as quantum dots that promise significantly greater fluorescence quantum yield.[33] We will implement these changes in the future MEMS prototype.

Acknowledgments

References

1. J. Pawley, Ed., *Handbook of Biological Confocal Microscopy*, 3rd ed., Plenum, New York (1996).
2. P. Anikijenko, L. T. Vo, E. R. Murr, J. Carrasco, W. J. McLaren, Q. Chen, S. G. Thomas, P. M. Delaney, and R. G. King, "*In vivo* detection of small subsurface melanomas in athymic mice using noninvasive fiber optic confocal imaging," *J. Invest. Dermatol.* **117**, 1442–1448 (2001).
3. L. T. Vo, G. D. Papworth, P. M. Delaney, D. H. Barkla, and R. G. King, "*In vivo* mapping of the vascular changes in skin burns of anaesthetised mice by fibre optic confocal imaging (FOCI)," *J. Dermatol. Sci.* **23**, 46–52 (2000).
4. P. J. White, R. D. Fogarty, I. J. Liepe, P. M. Delaney, G. A. Werther, and C. J. Wraight, "Live confocal microscopy of oligonucleotide uptake by keratinocytes in human skin grafts on nude mice," *J. Invest. Dermatol.* **112**, 887–892 (1999).
5. L. T. Vo, G. D. Papworth, P. M. Delaney, D. H. Barkla, and R. G. King, "A study of vascular response to thermal injury on hairless mice by fibre optic confocal imaging, laser doppler flowmetry and conventional histology," *Burns* **24**, 319–324 (1998).
6. L. J. Bussau, L. T. Vo, P. M. Delaney, G. D. Papworth, D. H. Barkla, and R. G. King, "Fibre optic confocal imaging (FOCI) of keratinocytes, blood vessels and nerves in hairless mouse skin in vivo," *J. Anat.* **192**, 187–194 (1998).
7. T. R. Corle and G. S. Kino, *Confocal Scanning Optical Microscopy and Related Imaging Systems*, Academic Press, Boston (1996).
8. D. L. Dickensheets and G. S. Kino, "Silicon-micromachined scanning confocal optical microscope," *J. MEMS* **7**, 38–47 (1998).
9. D. L. Dickensheets and G. S. Kino, "A micromachined scanning confocal optical microscope," *Opt. Lett.* **21**, 764–766 (1996).
10. T. D. Wang, M. J. Mandella, C. H. Contag, and G. S. Kino, "Dual-axis confocal microscope for high-resolution in vivo imaging," *Opt. Lett.* **28**, 414–416 (2003).
11. T. D. Wang, C. H. Contag, M. J. Mandella, N. Y. Chan, and G. S. Kino, "Dual axes confocal microscopy with post-objective scanning and low coherence heterodyne detection," *Opt. Lett.* (in press).
12. R. Y. Tsien, "The green fluorescent protein," *Annu. Rev. Biochem.* **67**, 509–544 (1998).
13. M. Chalfie, Y. Tu, G. Euskirchen, W. W. Ward, and D. C. Prasher, "Green fluorescent protein as a marker for gene expression," *Science* **263**, 802–805 (1994).
14. A. Wysocka and Z. Krawczyk, "Green fluorescent protein as a marker for monitoring activity of stress-inducible hsp70 rat gene promoter," *Mol. Cell. Biochem.* **215**, 153–156 (2000).
15. C. T. Baumann, C. S. Lim, and G. L. Hager, "Simultaneous visualization of the yellow and green forms of the green fluorescent protein in living cells," *J. Histochem. Cytochem.* **46**, 1073–1076 (1998).
16. Z. Xia and Y. Liu, "Reliable and global measurement of fluorescence resonance energy transfer using fluorescence microscopes," *Biophys. J.* **81**, 2395–2402 (2001).
17. S. M. Potter, C. M. Wang, P. A. Garrity, and S. E. Fraser, "Intravital imaging of green fluorescent protein using two-photon laser-scanning microscopy," *Gene* **173**, 25–31 (1996).
18. Z. F. Mainen, M. Maletic-Savatic, S. H. Shi, Y. Hayashi, R. Malinow, and K. Svoboda, "Two-photon imaging in living brain slices," *Methods* **18**, 231–239 (1999).
19. M. Zernicka-Goetz and J. Pines, "Use of green fluorescent protein in mouse embryos," *Methods* **24**, 55–60 (2001).
20. M. Zernicka-Goetz, J. Pines, S. McLean Hunter, J. P. Dixon, K. R. Siemering, J. Haseloff, and M. J. Evans, "Following cell fate in the living mouse embryo," *Development* **124**, 1133–1137 (1997).
21. M. Ikawa, K. Kominami, Y. Yoshimura, K. Tanaka, Y. Nishimune, and M. Okabe, "A rapid and non-invasive selection of transgenic embryos before implantation using green fluorescent protein (GFP)," *FEBS Lett.* **375**, 125–128 (1995).
22. R. M. Hoffman, "Visualization of GFP-expressing tumors and metastasis in vivo," *BioTechniques* **30**, 1016–1026 (2001).
23. R. M. Hoffman, "Green fluorescent protein imaging of tumour growth, metastasis, and angiogenesis in mouse models," *Lancet* **3**, 546–556 (2002).
24. S. Hasegawa, M. Yang, T. Chishima, Y. Miyagi, H. Shimada, A. R. Moossa, and R. M. Hoffman, "*In vivo* tumor delivery of the green fluorescent protein gene to report future occurrence of metastasis," *Cancer Gene Ther.* **7**, 1336–1340 (2000).
25. R. H. Webb and F. Rogomentich, "Confocal microscope with large field and working distance," *Appl. Opt.* **38**, 4870–4875 (1999).
26. S. Lindek and E. H. K. Stelzer, "Optical transfer functions for confocal theta fluorescence microscopy," *J. Opt. Soc. Am. A* **13**, 479–482 (1996).
27. E. H. K. Stelzer, S. Lindek, S. Albrecht, R. Pick, G. Ritter, N. Salmon, and R. Stricker, "A new tool for the observation of embryos and other large specimens: confocal theta fluorescence microscopy," *J. Microsc.* **179**, 1–10 (1995).
28. E. H. K. Stelzer and S. Lindek, "Fundamental reduction of the observation volume in far-field light microscopy by detection orthogonal to the illumination axis: confocal theta microscopy," *Opt. Commun.* **111**, 536–547 (1994).
29. R. Heim, D. C. Prasher, and R. Y. Tsien, "Wavelength mutations and posttranslational autoxidation of green fluorescent protein," *Proc. Natl. Acad. Sci. U.S.A.* **91**, 12501–12504 (1994).
30. A. K. Hadjantonakis, M. Gertsenstein, M. Ikawa, M. Okabe, and A. Nagy, "Generating green fluorescent mice by germline transmission of green fluorescent ES cells," *Mech. Dev.* **76**, 79–90 (1998).
31. E. Yeh, K. Gustafson, and G. L. Boulianne, "Green fluorescent protein as a vital marker and reporter of gene expression in *Drosophila*," *Proc. Natl. Acad. Sci. U.S.A.* **92**, 7036–7040 (1995).
32. M. Orihara, C. Hosono, T. Kojima, and K. Saigo, "Identification of engrailed promoter elements essential for interactions with a stripe enhancer in *Drosophila* embryos," *Genes Cells* **4**, 205–218 (1999).
33. W. C. Chan and S. Nie, "Quantum dot bioconjugates for ultrasensitive nonisotopic detection," *Science* **281**, 2016–2018 (1998).